Ferritic-Austenitic Solidification Mode in Austenitic Stainless Steel Welds

N. SUUTALA, T. TAKALO, AND T. MOISIO

The macro- and microstructures of about fifty different stainless welds of the AISI/AWS 300 series are analyzed. The results indicate that under conditions corresponding to a typical shielded metal arc (SMA) welding the welds with a ratio in the range $1.48 \lesssim Cr_{eq}/Ni_{eq} \lesssim 1.95$, where Ni_{eq} and Cr_{eq} are the nickel and chromium equivalents on the Schaeffler diagram, solidify in accordance with a duplex mode with the delta ferrite as the primary (leading) phase. The austenite forms between ferrite dendrites through a three-phase reaction between liquid, ferrite and austenite, and subsequently grows into the ferrite by either an equiaxial or an acicular mechanism, resulting in a drastic decrease in the volume fraction of the delta ferrite. The microstructure at room temperature is characterized by a general irregularity and the varied morphology of the ferrite. The compositional differences observed at room temperature are a consequence both of the solidification and the solid state transformation.

STAINLESS welds of the AISI/AWS 300 series can be classified into three types, *A*, *B* and *C*, according to their general microstructure and the morphology of the delta ferrite, as shown in our previous papers.[1-3] Type *A* welds, having a low Cr_{eq}/Ni_{eq}* ratio ($\lesssim 1.48$), solidify primarily as austenite, and the delta ferrite, if any, is formed from the rest melt between the austenite cells or dendrites and is always of a rounded appearance, *i.e.* a vermicular morphology, at room temperature (RT). Type *C* welds, having a high Cr_{eq}/Ni_{eq} ratio ($\gtrsim 1.95$), solidify as single-phase ferrite. The austenite nucleates only in the solid state, preferentially at ferrite grain boundaries, and grows into the ferrite by the Widmanstätten mechanism during cooling, resulting in a lathy morphology. The volume fraction of residual ferrite at RT increases with the ratio Cr_{eq}/Ni_{eq}, until it becomes the ferrite which forms the matrix at values above 2.3.

*Cr_{eq} = Cr + Mo + 1.5 Si + 0.5 Nb. Ni_{eq} = Ni + 30 C + 0.5 Mn.

In this third part of the work the microstructural type *B* is discussed more thoroughly against the same general and experimental background.[2] On a tonnage basis, this is the most important type in view of certain beneficial properties associated with it.

RESULTS

Complete welding parameters for the test welds are given in Table I, and the rest of the routine for preparing the specimens is as described earlier.[2] Only welds which belong to the microstructural type *B* or contain areas of type *B*, *i.e.* welds numbers *B*1 through *B*26, *A*15 and *C*5 are considered here (see Tables II and III). The ferrite content of these welds normally ranged from 4 to 18 pct increasing with the ratio Cr_{eq}/Ni_{eq} (Fig. 1). Roughly it is between those of type *A* and *C* welds. The exact compositions of the welds in question are given in Table II. When plotted on the Schaeffler diagram[4] these fell within a sharply outlined field approximately defined by the ratio range $1.48 \lesssim Cr_{eq}/Ni_{eq} \lesssim 1.95$ (Fig. 2).

The fact that welds numbers *B*1 and *B*2 are located beyond the ordinary field for type *B* welds (Fig. 2) may be explained by their exceptional composition, for the coefficients for nitrogen and manganese in the Ni_{eq} and Cr_{eq} of the Schaeffler and DeLong diagrams[5] are probably too great for such high alloying levels[6] (*B*1: N = 0.17 pct, *B*2: Mn = 8 pct). Their ferrite contents, 1.5 and 3 pct respectively, are also

Table I. Welding Conditions

SMA Welds in the First and Second Series			
Electrode diameter (mm)	2.5	3.25	4.0
Welding current (A)	60 to 80	80 to 110	120 to 140
Heat input (kJ/cm)	6 to 8	7 to 9	11 to 16
Interpass temperature	<100°C		
Polarity	DC, reverse		
Welding position	Flat		
Technique	Manual stringer bead		
GTA Welds in the First Series			
Filler metal	None		
Welding current	190 A*		
Pole voltage	14 to 17 V*		
Travel speed	8 cm/min		
Heat input	17 to 21 kJ/cm*		
Arc length	2.0 mm		
Thoriated tungsten electrode	EWTh-2, diameter 3.2 mm and cone angle 90 deg		
Shielding gas	Welding grade argon, flow 8 l/min		
Torch position	Vertical, orifice diameter 11 mm and distance from the plate 10 mm		
Polarity	DC, straight		
Welding position	Flat		
Technique	Mechanised stringer bead		

*These values are valid for the plates of thickness 16 mm. In the case of thinner plates the current was reduced to a value such that the energy equivalent $Q/\sqrt{2s}$ remained unchanged (Q = heat input = current · arc voltage/speed and s = plate thickness).

N. SUUTALA and T. MOISIO are Research Staff Member and Head, respectively, Laboratory of Physical Metallurgy, University of Oulu, Oulu, Finland, and T. TAKALO, formerly Research Staff Member, Laboratory of Physical Metallurgy, University of Oulu, is now Research Engineer, Outokumpu Company, Tornio, Finland.

Manuscript submitted September 21, 1979.

ISSN 0360-2133/80/0512-0717$00.75/0

Table II. Codes of the Experimental Welds in the First and Second Series, Types of Filler and Base Metals According to AISI, AWS and ACI Specifications and Chemical Compositions (Analyzed by Outokumpu Oy, Stainless Steel Group). Welds Which Do Not Fit These Specifications are Marked "Electrode" and "Wrought". The Calculated Chromium and Nickel Equivalents, Cr_{eq} = Cr + Mo + 1.5 Si + 0.5 Nb, Ni_{eq} = Ni + 30 C + 0.5 Mn, and the Measured Percent Ferrite are Given in the Last Two Columns

Code	Type	Composition of Deposited Weld Metals, Wt Pct									Equivalents		Percent¶ Ferrite
		C	Si	Mn	P	S	Cr	Ni	Mo	Others	Cr_{eq}	Ni_{eq}	
						First Series							
*B*1	304LN	0.025	0.38	1.40	0.034	0.008	18.9	8.9	0.35	0.165 N†	19.8	13.6	0.7–1.8
*B*2	Electrode	0.030	0.42	(8)	–	–	17.3	8.9	0.06	–	18.0	14.0	2.6–3.6
*B*3	304L	0.026	0.59	1.18	0.023	0.010	18.8	10.9	0.25	–	19.9	12.3	3.8–4.5
*B*4	304	0.055	0.66	1.58	0.023	0.007	18.8	9.1	0.18	–	20.0	11.5	4.1–6.6
*B*5	321	0.06	0.58	1.50	0.028	0.013	17.8	10.3	0.45	0.6 Ti‡	20.3	12.9	5.4–5.9
*B*6	304	0.039	0.44	1.52	0.034	0.006	19.2	8.7	0.44	–	20.3	10.6	5.6–5.9
*B*7	316	0.042	0.40	1.64	0.031	0.010	17.1	10.8	2.5	0.058 N†	20.2	12.9	5.6–6.5
*B*8	316L	0.026	0.68	1.58	0.046	0.022	16.8	11.5	3.0	–	20.8	13.1	8.2–8.6
*B*9	E347-16	0.057	0.66	1.24	0.017	0.008	19.3	9.7	0.03	0.61 Nb	20.6	12.0	7.1–10.0
*B*10	E316-15	0.046	0.40	0.70	0.016	0.008	18.8	12.2	2.7	–	22.2	13.9	7.8–10.5
*B*11	Wrought	0.024	0.87	1.36	0.027	0.007	20.7	15.1	3.0	0.26 Cu	25.0	16.6	9.1–9.7
*B*12	E308L-15	0.028	0.87	0.65	0.021	0.007	19.4	9.5	0.09	–	20.8	10.7	9.0–10.7
*B*13	E316L-15	0.030	0.92	0.72	0.018	0.009	18.6	12.3	2.9	0.041 N†	22.9	13.6	10.2–11.5
*B*14	E347-16	0.054	0.61	1.22	0.023	0.009	19.6	9.6	<0.01	0.78 Nb	20.9	11.8	10.2–11.6
*B*15	E308L-16	0.026	0.88	0.60	0.019	0.008	20.8	10.5	0.03	–	22.2	11.6	9.2–12.9
*B*16	E318-16	0.032	0.66	1.40	0.016	0.009	18.2	12.0	2.9	0.60 Nb	22.4	13.7	10.6–12.8
*B*17*	CF-8M	0.07	0.47	0.81	0.021	0.010	18.2	9.9	2.4	–	21.3	12.3	12.7–14.0
*B*18	E347-16	0.018	0.93	0.70	0.016	0.008	21.6	11.3	0.01	0.30 Nb	23.2	12.2	12.5–17.3
*B*19	E309-15	0.09	0.70	1.65	0.032	0.010	25.1	12.5	0.08	0.091 N†	26.2	15.9	12.2–16.2
*B*20	E309Mo-16	0.025	1.14	1.33	0.021	0.006	20.3	13.3	2.5	–	24.5	14.7	14.5–17.0
*B*21	E309-15	0.046	0.43	2.9	0.022	0.006	23.4	11.4	0.47	–	24.5	14.2	17.5–19.7
*B*22	E312-16	0.09	0.61	1.90	0.023	0.009	28.5	11.0	0.31	–	29.7	14.5	42–44
						Second Series							
*B*23	E316L-16	0.032	0.75	0.77	0.028	0.013	18.5	12.0	2.7	–	22.3	13.3	7–9
*B*24	E308L-15	0.035	0.93	0.70	0.014	0.007	19.2	9.3	0.03	–	20.6	10.7	7–9
*B*25	E308L-16	0.034	0.94	0.79	0.037	0.010	19.6	10.1	0.02	–	21.0	11.5	7–10
*B*26	E347-16	0.026	0.92	0.92	0.022	0.009	21.2	10.4	0.23	0.27 Nb	23.0	11.6	9–15
*A*15*	Electrode	0.030	0.88	1.01	0.017	0.007	17.3	14.5	4.6	–	23.2	15.9	7.2–8.7
*C*5*	(E309Mo-16)	0.027	0.68	0.96	0.020	0.008	21.5	12.2	2.3	–	24.8	13.8	18.3–20.5

*Weld numbers A15 and C5 partially of type *B*, weld number *B*17 partially of type C.

†The nitrogen content given in the column "others" was determined only in those four welds. This nitrogen was not included in the nickel equivalent, except in the weld of N-alloyed grades (weld number *B*1), for which the equation Ni_{eq} = Ni + 30 C + 30 (N–0.06) + 0.5 Mn was used (see Ref. 5).

‡ The equation Cr_{eq} = Cr + Mo + 1.5 Si + 0.5 Nb + 2 Ti was used (see Ref. 6).

¶ Measurements were carried out by the permeability method (Fisher's Permascope), except in weld number *B*22, where they were performed metallographically.

Table III. Methods of Metallographic Analysis

Ferrite content measurements	All welds
Light microscopy	All welds
Scanning electron microscopy	Welds numbers *A*15, *B*1, *B*3, *B*5, *B*7, *B*10, *C*5
Transmission electron microscopy	Welds numbers *B*3, *B*5, *B*9
Electron probe microanalysis	Welds numbers *A*15, *B*5, *B*7, *B*23, *B*25, *C*5
X-ray texture measurements	Welds numbers *B*19, *B*21, *B*22, *B*23, *B*24, *B*25, *B*26

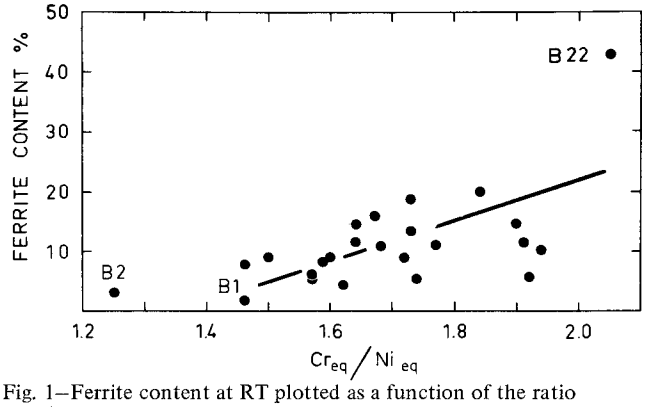

Fig. 1–Ferrite content at RT plotted as a function of the ratio Cr_{eq}/Ni_{eq}.

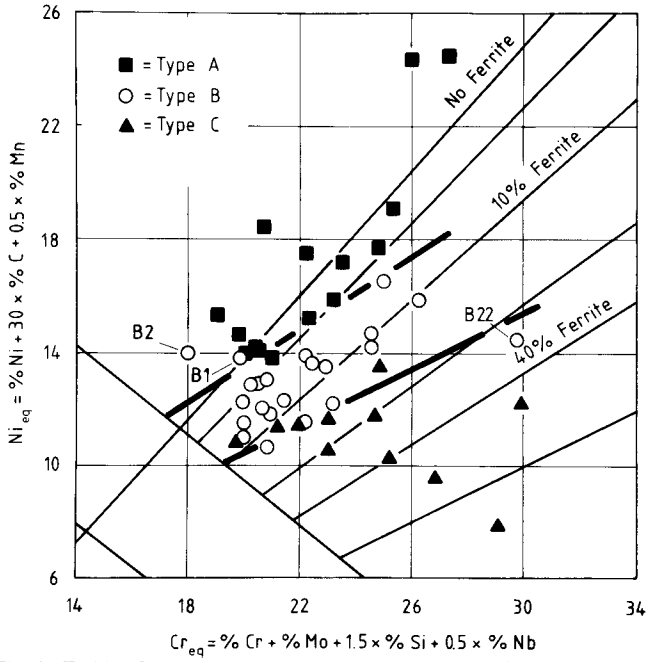

Fig. 2–Fields of the microstructural types in the Schaeffler diagram.

higher than values predicted by the diagrams, although they do not differ markedly from those of other welds in this group. The third exceptional weld is number *B*22, the ferrite content of which, 40 pct, is much higher than normal (Fig. 1). The microstructure of this weld also possesses some exceptional features.

The microstructure of type *B* welds is difficult to describe. In fact, irregularity seems to be its most conspicuous feature at low magnifications under a light microscope. This is basically a consequence of the lack of self-evident growth units, but is also partially due to the finely dispersed duplex austenitic-ferritic structure. This irregularity is not so distinctive at higher magnifications.

The microstructure is highly variable depending on the composition, and possesses some features in common with types *A* and *C*. The vermicular morphology of the delta ferrite is dominant at low values of the ratio Cr_{eq}/Ni_{eq}, the structure having dendritic features (Figs. 4(*a*) and 5). The proportion of lathy ferrite increases as the ratio Cr_{eq}/Ni_{eq} increases, as established quantitatively in Fig. 3. The lathy ferrite is not located inside large grains, but as "packs" with the size of an order smaller than in type *C* welds (Figs. 4(*b*) and 6). Sometimes such packs occur side by side with vermicular ferrite, and sometimes they fill wide areas. In the latter case the existence of lathy ferrite in the sections concerned gives a network appearance (Fig. 6).

The delta ferrite is located indisputably on the axes of cells or cellular dendrites, when the ratio Cr_{eq}/Ni_{eq} is high *i.e.* 1.7 to 1.95 (see Fig. 4(*b*)), whereas only a careful metallographic analysis will reveal that the ferrite is located mainly at dendrite axes even at low values of the ratio Cr_{eq}/Ni_{eq} (~ 1.5) and not between them as in type *A* welds. Some welds of type *B* also contain a small proportion of roundish or inclusion-like ferrite in the interdendritic regions (see Fig. 5), but its amount is probably insignificant compared with the total ferrite content.

The dimensions of the solidification substructure outlined on the basis of the ferrite strings are somewhat greater than in type *A* and *C* welds. The primary arm spacing was 20, 25 and 30 μm respectively in welds numbers *B*7, *C*5 (type *B* areas) and *B*22, for instance. Generally, the ferrite seems to become coarser with a decrease in iron content, *i.e.* with an increase in the sum $Cr_{eq} + Ni_{eq}$. The structure then exhibits colonial-like features, as are shown most clearly in weld number *B*22 (Fig. 4(*c*)) and are also distinguishable to some extent in welds numbers *B*19, *B*20 and *B*21. In weld number *B*22 both the sum and ratio of equivalents are very high, and this contains areas of uniform, *i.e.* untransformed, ferrite (Fig. 4(*c*)).

Concentration profiles* from the type *B* structure

*The EPMA study was carried at 20 kV using a minimum beam diameter (~1 μm) with a step length of 0.667 μm. For quantitative calibration, the average net X-ray intensity obtained from the microprobe analysis was equalized with the content analyzed by spectrometers, followed by a linear approximation. After that, the profiles were smoothed mathematically by a computer in order to elucidate the periodicity generated by solidification and to facilitate the estimation of segregation ratios. Thus each point in Fig. 7 was the arithmetical mean of three successive steps and in Fig. 8 of five such steps, *i.e.* the profile was averaged over distances of 2 μm and 3.33 μm. The partition ratios presented in Table IV, however, were calculated on the basis of the original concentration profiles, without smoothing.

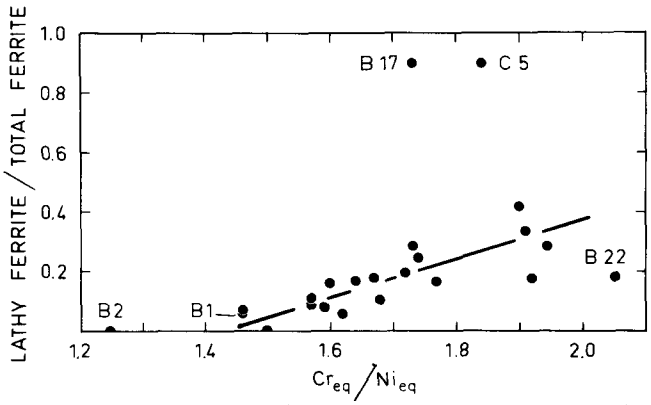

Fig. 3—Effect of the ratio Cr_{eq}/Ni_{eq} on the proportion of lathy ferrite in the type *B* structure. The rest of ferrite vermicular, except in weld number *B*22, where it is untransformed (see text). Values were determined using the metallographic point counting method (thirty fields per weld).

by the EPMA method indicate an entirely different distribution of alloying elements from that found in type *A* welds, but principally a similar distribution to that occurring in type *C* welds. The interdendritic regions are depleted in Cr and enriched in Ni, and to a lesser extent in Mo, Si, and Mn (Figs. 7 and 8). The apparent segregation ratios ($C_{interdendritic}/C_{dendritic}$) for Si, Mn, Cr, Ni and Mo can be estimated on the basis of these profiles, and some values are presented in Table IV. The real compositional differences are greater due to the partitioning in the duplex structure, since the ferrite is additionally enriched in "ferritizers" and depleted in "austenitizers", as is also shown in Table IV. Examination of Fig. 7, where the line of analysis also crosses a small particle of interdendritic ferrite, results in the assumption that the interdendritic ferrite differs

Table IV. Microsegregation and Partitioning of Alloying Elements Between Austenite and Ferrite in Type *B* Structure Estimated on the Basis of the EPMA Analysis

Weld Number	Cr_{eq}/Ni_{eq}	Si	Mn	Cr	Ni	Mo	Ferrite Morphology
			Segregation ratio S				
*A*15	1.53	0.9	1.0	0.95	1.0	0.8	Vermicular
*B*7	1.57	1.0	0.9	1.0	1.3	1.0	Vermicular
*C*5	1.84	–	–	0.95	1.2	1.1	Lathy
			Partition ratio P_D				
*A*15	1.53	1.1	0.9	1.1	0.8	1.1	Vermicular
*B*7	1.57	1.2	1.0	1.1	0.9	1.2	Vermicular
*C*5	1.84	–	–	1.05	0.9	1.15	Lathy
			Partition ratio P_{ID}				
*B*7	1.57	1.2	1.05	1.05	0.8	1.25	Vermicular

Segregation ratio S = ratio of the concentration of an element in the interdendritic areas to that at the center of the dendrites.

Partition ratio P_D = ratio of the concentration of an element in dendritic ferrite to that in adjacent austenite.

Partition ratio P_{ID} = ratio of the concentration of an element in interdendritic ferrite to that in adjacent austenite.

Note: The electron probe beam diameter (~1 μm) is one order smaller than the segregation distance, but of the same order as the thickness of the delta ferrite particles. Consequently the estimated values for S are unaffected, but the true partitioning is more extensive than shown above. The values for P_D and P_{ID} measured in the different welds are intercomparable, however.

in composition from the dendritic ferrite (having a higher Ni content). Statistically, this statement is not very reliable, however, because of the small number of observations.

The TEM study was carried out on welds numbers *B*3, *B*5 and *B*9, which all have a relatively low Cr_{eq}/Ni_{eq} ratio and thus exhibit mainly a vermicular morphology for the delta ferrite. Figure 9 depicts round-

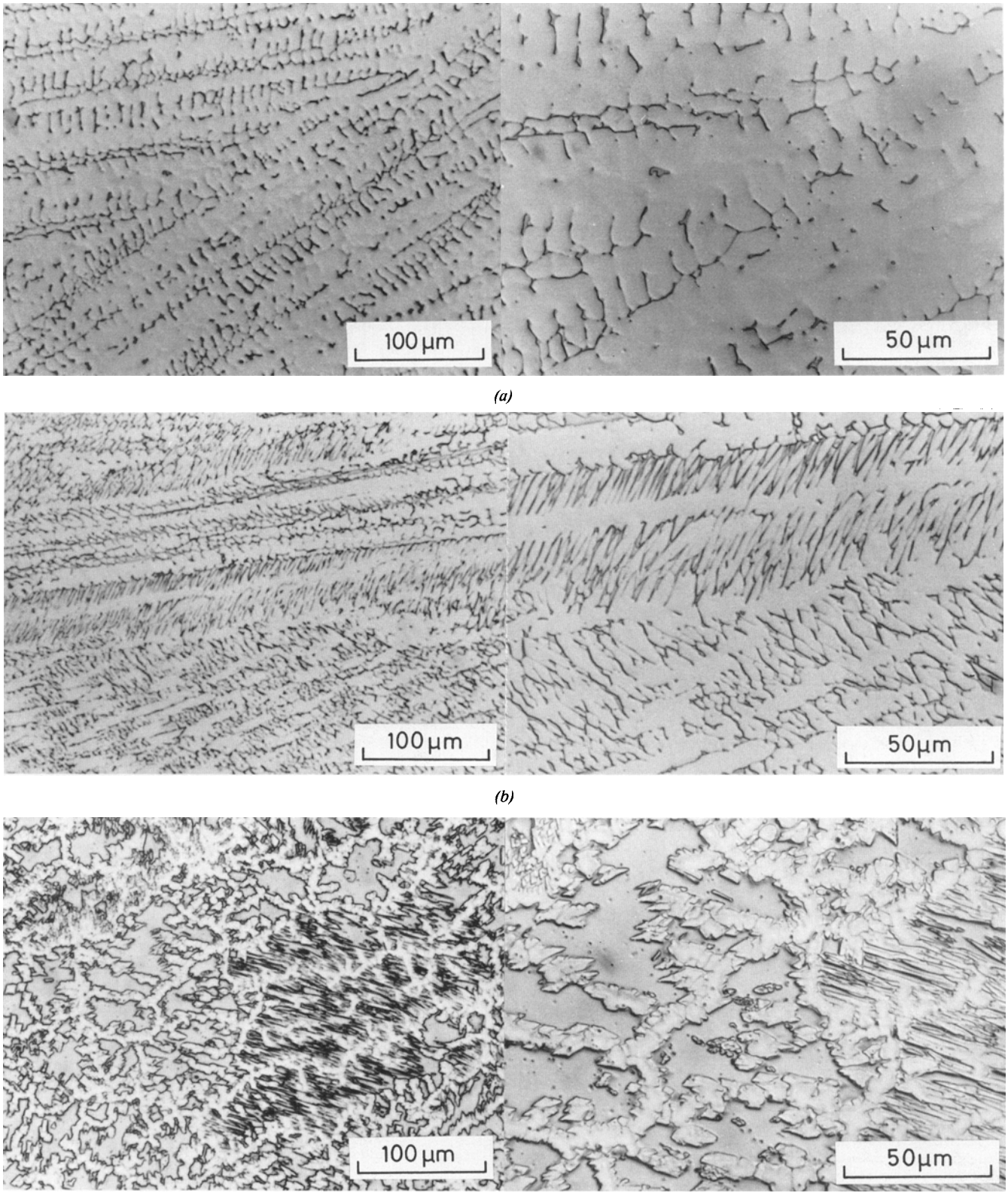

Fig. 4—Typical microstructures in type *B* welds at different values of the ratio Cr_{eq}/Ni_{eq}: (*a*) Cr_{eq}/Ni_{eq} = 1.62, vermicular morphology is dominant (weld number *B*3, Cr_{eq} = 19.9, Ni_{eq} = 12.3); (*b*) Cr_{eq}/Ni_{eq} = 1.73, more lathy morphology exists than in (*a*) (weld number *B*17, Cr_{eq} = 21.3 Ni_{eq} = 12.3); and (*c*) Cr_{eq}/Ni_{eq} = 2.05, fraction of undecomposed ferrite is high (weld number *B*22, Cr_{eq} = 29.7, Ni_{eq} = 14.5).

ish shapes typical of vermicular ferrite. Diffraction work showed that no distinct orientation relationship holds between the austenite and vermicular ferrite similar to that found in type *A* welds, although a relationship close to the standard *K-S* or *N-W* relationships was found to exist between austenite and the lathy ferrite, detected occasionally in weld no. *B*3. In this respect the results are consistent with those obtained from type *C* welds, allowing the conclusion that the orientation relationship seems to be a general feature of the lathy morphology both in type *C* and in type *B* welds.

The results of X-ray texture measurements made from certain multirun welds (Table III) in which the intensity (*i.e.* the volume fraction of ferrite) was high enough for such measurements, indicate a simple [100] texture for the delta ferrite, while the austenite has two alternative orientations, either a [100] direction (strong) or a [110] direction, being parallel to the normal of the surface. The relative intensity of the latter increased from "very weak" to "weak" with an increase in the ratio Cr_{eq}/Ni_{eq}. In one exceptional case (weld number *B*22) the austenite and ferrite had an exactly similar [100] texture, *i.e.* the intensity maxima of both phases occurred at the same angular values in the pole figure.

DISCUSSION

Solidification

Both the solidification behavior and the mechanism of ferrite decomposition in austenitic stainless welds are governed by the balance between austenite-form-

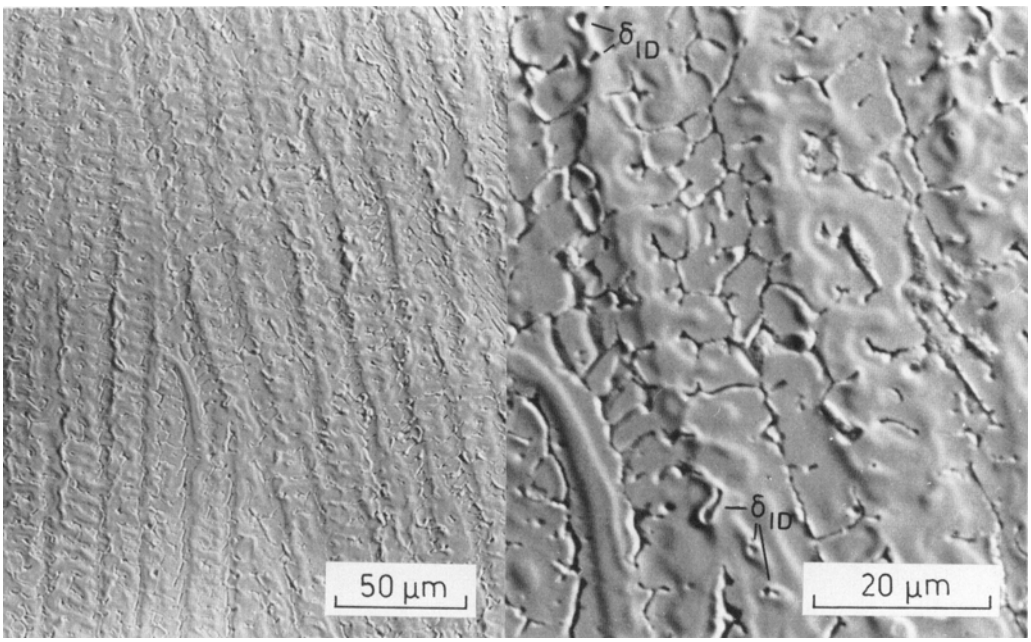

Fig. 5—SEM micrograph in weld number *B*7 of type 316 (Cr_{eq} = 20.2, Ni_{eq} = 12.9, ferrite content 6 pct). Some interdendritic ferrite particles are labelled by the letters δ_{ID}.

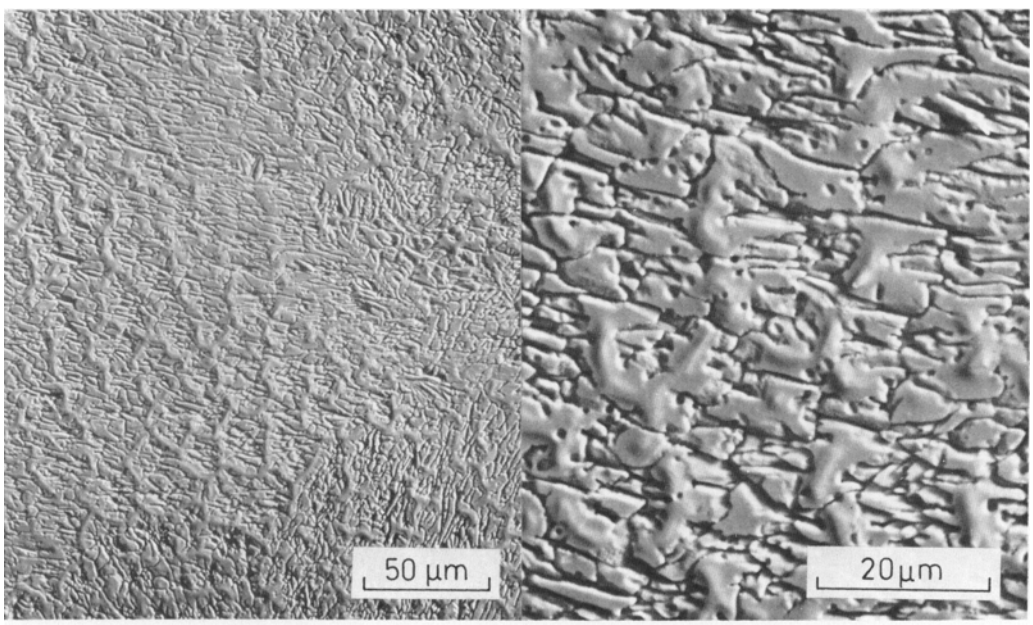

Fig. 6—SEM micrograph in areas of type *B* in weld number *C*5 of type E309Mo-16, (Cr_{eq} = 24.8, Ni_{eq} = 13.5, ferrite content 19 pct).

ing and ferrite-forming elements, and their influence can be described by the appropriate expressions for Cr_{eq} and Ni_{eq}. Low values for the ratio Cr_{eq}/Ni_{eq} result in the austenitic solidification mode and the type *A* microstructure, and high values in the single-phase ferritic solidification mode and type *C* microstructure. The type *A* can be easily identified on the basis of the well-retained solidification substructure and the type *C* on the basis of the Widmanstätten structure caused by the phase transformation of $\delta \rightarrow \gamma$ in the solid state.[1-3]

Identification of the type *B* microstructure and the exact interpretation of its history is more difficult. This type has some features in common with both other types, and it is obviously affected both by the solidification and the decomposition of the ferrite, as proposed in one of our earlier communications.[1] The location of the ferrite on dendrite axes (Figs. 4 through 6) suggests the primacy of the ferrite in type *B* welds. Also a look at the ternary Fe-Cr-Ni phase diagrams allows the possibility of a ferritic-austenitic solidification mode between the austenitic and single-phase ferritic ones (see Fig. 10). This

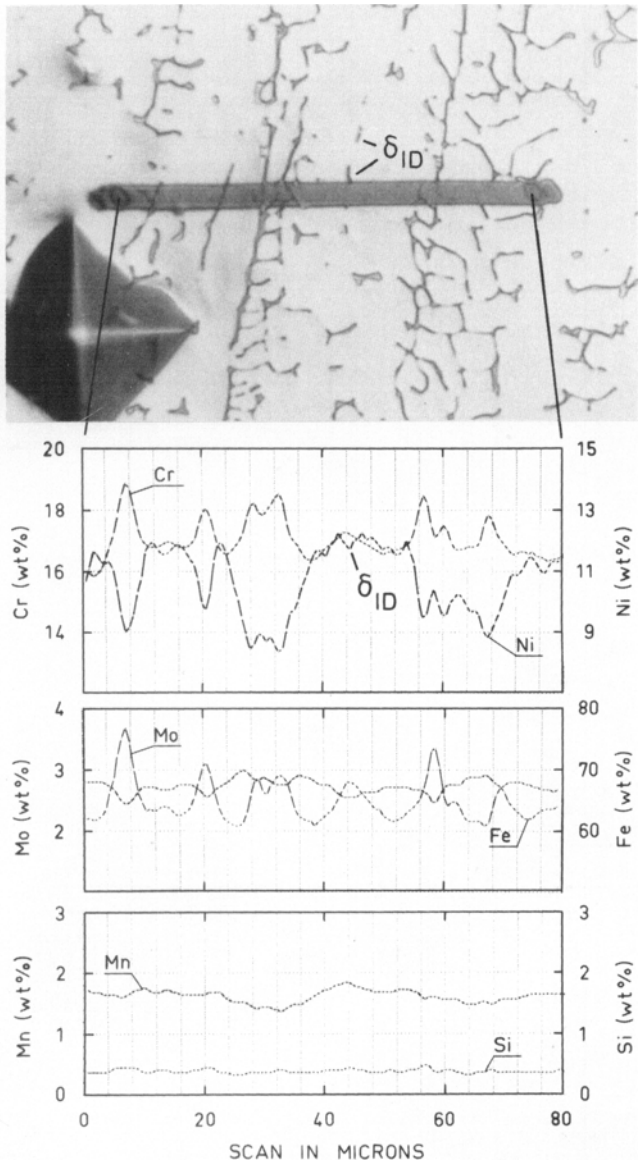

Fig. 7—Concentration profiles for Si, Mn, Cr, Ni, Mo, and Fe across two primary ferrite dendrites and one interdendritic ferrite particle in the same weld as in Fig. 5. For the analysis technique, see footnote in the text.

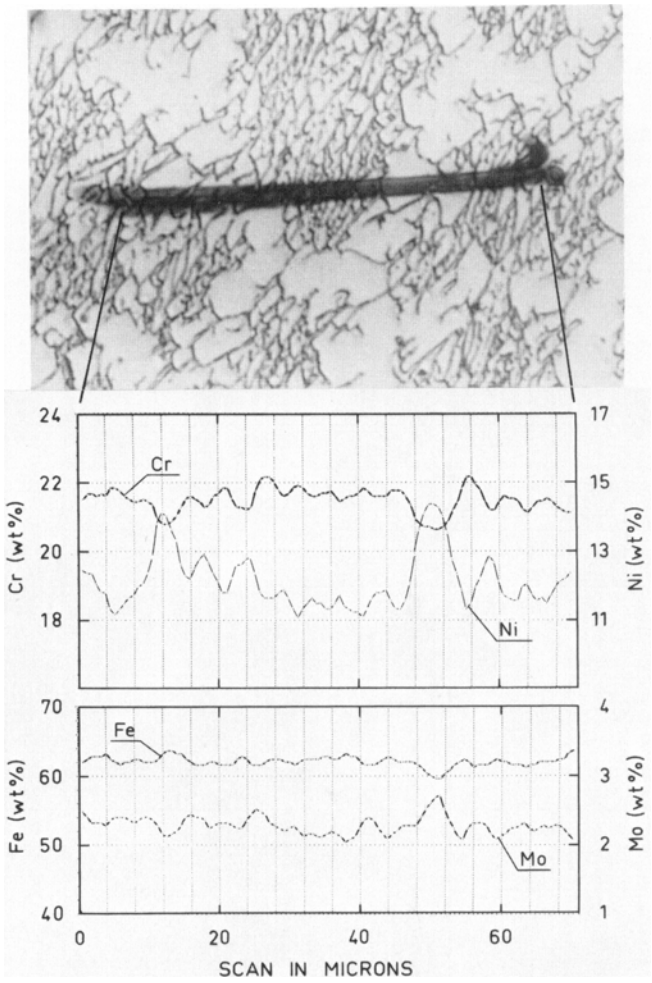

Fig. 8—Concentration profiles for Cr, Ni, Mo, and Fe across a "pack" of lathy ferrite in the same weld as in Fig. 6. For the analysis technique, see footnote in the text. Profiles were smoothed more than in Fig. 7.

Fig. 9—Thin foil micrograph illustrating vermicular ferrite (δ) and austenite (γ) in the same weld as in Fig. 4(*a*).

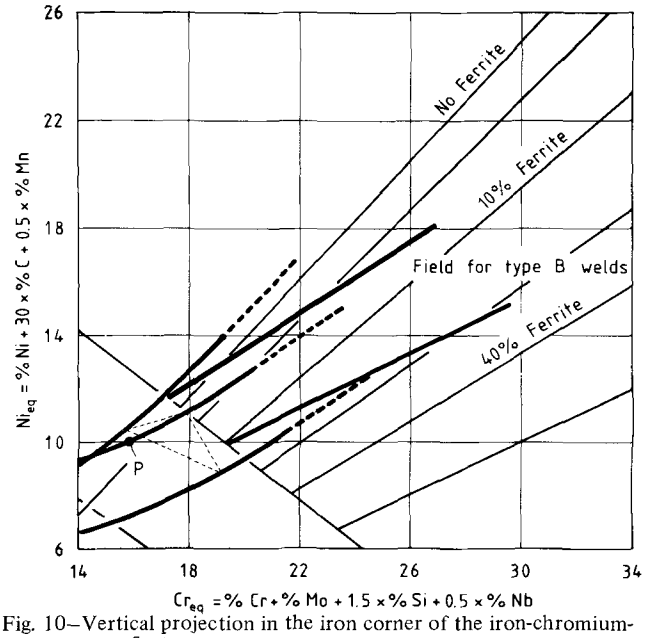

Fig. 10—Vertical projection in the iron corner of the iron-chromium-nickel system,[7] representing the melting equilibria drawn on the conventional Schaeffler diagram. The point P corresponds to the transition from peritectic to eutectic solidification.

statement is supported most strongly by the results of the EPMA study, however.

The distribution of alloying elements can be clarified by plotting* composition paths on the Cr_{eq}-Ni_{eq} co-ordinates (Fig. 11). In single-phase structures of types *A* and *C* the direction of such a path demonstrates the direction of a tie line, provided that the homogenization does not twist it. This is approximately true, for the diffusion coefficients of the main alloying elements Cr, Ni and Mo are of the same order, at least in the binary systems of iron.[8] Thus the length of the path is only shortened by homogenization. In two-phase structures, *e.g.* in all welds of type *B*, partitioning during the decomposition of ferrite has additional effects which are opposed to those of homogenization, and consequently the interpretation of Fig. 11 is as follows:

Firstly, Fig. 11 indicates that the directions of the tie lines in single-phase structures of type *A* and *C* are very different. In the former case Ni and Cr are segregated in the same phase, *i.e.* the tie lines are almost parallel to the borderline between the fields of type *A* and *B* welds, whereas in the latter they run in the opposite phase (tie lines being almost perpendicular to the borderline). Secondly, the length of the composition paths is much shorter in the type *C* structure than in type *A* because of the pronounced homogenization associated with the single-phase ferritic solidification (the diffusion coefficients are 100 times larger in ferrite than in austenite).[8] Thirdly, the composition paths in structures of types *A* and *B* have very different orientations, which cannot be explained by the effects of partitioning (see Table IV). In fact, the paths in the type *B* structure are parallel with those in the type *C* structure. This indicates clearly that the type *B* welds solidify in a ferritic-austenitic manner. The observations on the different directions of the tie lines in the austenitic and ferritic modes of solidification are consistent with the descriptions "gleichsinnige" und "ungleichsinnige Seigerung" given by Siegel and Günzel.[9]

As can be determined from Figs. 7, 8 and 11, the axes on ferrite dendrites are initially slightly enriched in Cr, but depleted in Ni. Coring during freezing results in an enrichment of "austenitizers", especially of Ni, in the interdendritic liquid, followed by a three-phase reaction between the liquid, delta ferrite and austenite. On the basis of the Fe-Cr-Ni phase diagrams (Fig. 10) this reaction is often referred to as eutectic in welds, *e.g.* in references.[10,11] However, Fredricksson[12,13] and Leffler and Malm[14] have shown with interrupted tests concerning directional solidification of steels of types 304 and 316 that austenite is normally formed between ferrite dendrites through peritectic reaction and transformation, and Fredriksson[13] has proposed that solidification changes from peritectic to eutectic once the contents of alloying elements are high enough. In the present series colonial-like eutectic features were detected only in weld number *B*22 (Fig. 4(*c*)), and some similarities could be observed in welds numbers *B*19, 20 and 21, *i.e.* those with very high values for the sum Cr_{eq} + Ni_{eq}. Elsewhere the ferrite was dendritic. This transition in the microstructure and the concentration profiles allow a peritectic reaction at low values of the sum Cr_{eq} + Ni_{eq}, but the definite solution of this problem is difficult on the microstructural basis.

The nonequilibrium growth of the austenite into the rest melt and ferrite causes segregation typical of austenitic solidification, *i.e.* the rest melt is enriched in all alloying elements except iron. Thus the formation of secondary ferrite is also possible in type *B* welds in last interdendritic regions to solidify, through a eutectic reaction, in a similar manner to that in which the ferrite is formed in type *A* welds.

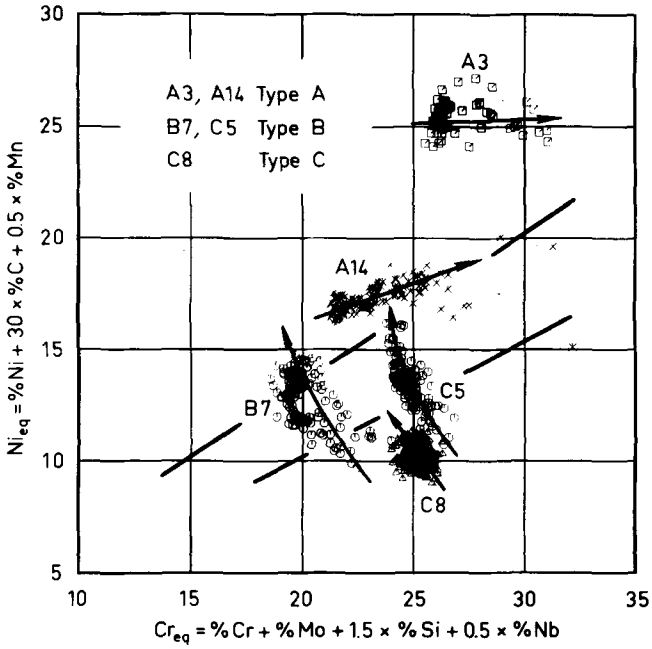

Fig. 11—Composition paths in the Schaeffler diagram. The structure in which paths are determined was single-phase austenitic in weld number *A*3, single-phase ferritic in number *C*8 and duplex in others.

*The Cr_{eq} and Ni_{eq} were calculated by a computer point by point on the basis of quantitative results obtained in the manner described in the previous footnote to the text. The carbon content was assumed to be constant and equal to that presented in Table II.

Corresponding segregation patterns can be distinguished around interdendritic ferrite particles (Fig. 7).

Decomposition of Delta Ferrite and Microstructure at Room Temperature

Independently of the character of the solidification, the ferrite becomes unstable compared with the austenite with decreasing temperature. The mechanism of the decomposition is affected by the chemical analysis. The higher the ratio Cr_{eq}/Ni_{eq}, the higher the maximum volume fraction of the ferrite and the lower the starting temperature of the transformation compared with the liquidus temperature. Thus high values for the ratio Cr_{eq}/Ni_{eq} result in more pronounced supercooling of the ferrite and consequently in the operation of the Widmanstätten mechanism and in the augmented proportional fraction of the lathy ferrite at RT (Fig. 3). The low values result in turn in the vermicular morphology due to the smaller supercooling and to the equiaxial growth mechanism, as it can be concluded by the inverse argument. The existence of both morphologies in the same weld, which is the normal case, can easily be explained by a size effect of the initial ferrite areas, the small areas decomposing by an equiaxial mechanism and the large ones by an acicular one.

The decomposition of the ferrite leads to the partitioning of alloying elements between austenite and ferrite. The values for the partition ratios P_D given in Table IV show the partitioning to be surprisingly independent of the morphology of the residual ferrite. This indicates that the decomposition of the ferrite takes place at relatively high temperatures even in those type *B* welds which contain large amounts of lathy ferrite at RT.

In the quantitative treatment of the distribution of alloying elements at RT attention must be paid to the fact that the segregation, homogenization and partitioning all have effects of their own on type *B* welds. The superimposed effect of the segregation and homogenization can be estimated to a certain extent on the basis of the segregation ratios, but the true partitioning is significantly more extensive than that shown in Table IV, as the electron probe beam diameter used is of the same order as the thickness of the delta ferrite particles. The calculated values for P_D reported in Table V, which summarized results obtained using high resolution scanning transmission microscopy (STEM), do in fact deviate more from unity than those determined in the present work (Table IV). In many cases the minimum (or maximum) content of certain elements is nevertheless of greater practical importance than the amplitude of the compositional variations.[19] For example, if one considers two welds of different heats of type 316 with the same nominal content of molybdenum, but assumes one of these to have a type *B* microstructure and the other type *A*. The minimum Mo content will be lower in the type *A* weld than in that of type *B*, due principally to the different distribution of alloying elements (see Figs. 7 and 8, and compare Fig. 8 in Ref. 2).

The results of texture measurements agree with the model presented above. The simple [100] texture of the ferrite is due entirely to the solidification. The austenite has a strong [100] component showing growth into the melt to be important, whereas the weak [110] component at high values of the ratio Cr_{eq}/Ni_{eq} is perhaps associated with the crystallography of the decomposition of the delta ferrite by an acicular mechanism. The exactly similar texture of the ferrite and austenite in weld number *B*22 may indicate coupled growth, *i.e.* eutectic solidification, as inferred on the basis of its colonial-like microstructure (Fig. 4(*c*)).

In a very recent paper Lyman[16] proposes that the ferrite transforms to austenite in a massive manner in a GTA weld of type 304L. Our results show that this transformation is controlled by diffusion, and that it is not massive in character at cooling rates typical of arc welding.

Table V. Partitioning of Alloying Elements Between Austenite and Ferrite in Type *B* Structure Calculated on the Basis of Results Reported from Analytical STEM Studies

		Partition Ratio P_D				
Author	Material	Cr_{eq}/Ni_{eq}	Cr	Ni	Mo	Ferrite Morphology
Åström *et al*[15]	E308	1.58	1.4	0.5	–	Vermicular
Lyman[16]	304L	1.80	1.3	0.6	–	Vermicular
Kyrölainen[17]	E309MoL	1.58	1.4	0.4	2.2	Vermicular
Kyrölainen[18]	ER318	1.73	1.4	0.4	1.8	Vermicular

Weld Properties and Microstructure

Most consumables of the AISI/AWS 300 series are designed (alloyed) so that the ferrite content of the weld metal at RT is from 5 to 10 pct, which agrees well with features of type *B* microstructure in our classification. Many good properties are related to this range of ferrite content: These welds have a minimum susceptibility to hot cracking and fissuring[20,21] and a satisfactory resistance to corrosion, except under certain severe conditions.[22,23]

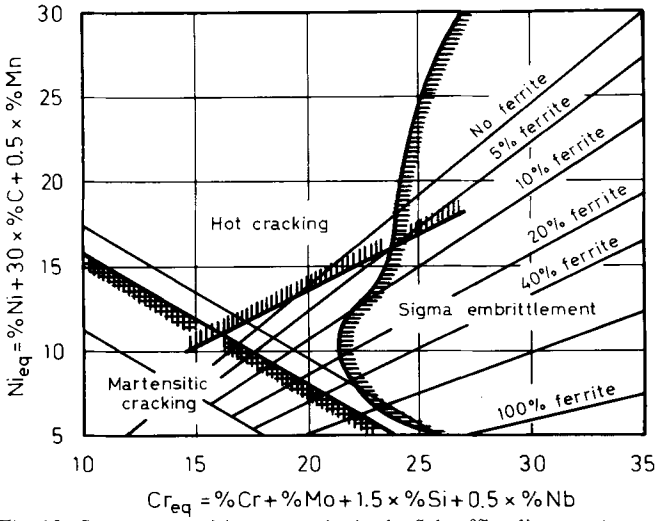

Fig. 12–Structure-sensitive properties in the Schaeffler diagram, *i.e.* middle parts of the Bystram diagram,[24] modified by reference to recent results concerning the borderline of hot-cracking sensitive welds.[2,21]

Brittle martensite is not normally formed in the microstructure, and at this level the ferrite does not reduce the ductility of untreated welds. In high-temperature service and during improper heat treatment, however, the ferrite accelerates transformation to the embrittling sigma phase.[22-24]

To summarize, the main dangers which restrict the weldability and usable composition field of stainless steel welds can be represented conveniently on the Bystram diagram (Fig. 12). Here the borderlines of the "cracking fields" originate from reference;[24] we have modified only the demarcation between hot-cracking sensitive and insensitive welds in agreement with our recent results.[2,21] Figure 12 isolates a "triangle" with the minimum danger. Comparison, with Fig. 2 shows that this is located inside the region of type *B* welds.

SUMMARY

The microstructures and macrostructures of about fifty different welds of the AISI/AWS 300 series are analyzed, and three microstructural types *A*, *B* and *C* set up.

Type *B* includes those welds with a moderate ferrite content in which the ratio Cr_{eq}/Ni_{eq} is approximately within the limits $1.48 \lesssim Cr_{eq}/Ni_{eq} \lesssim 1.95$, where Ni_{eq} and Cr_{eq} are the nickel and chromium equivalents on the Schaeffler diagram. Their general structure is very irregular. The delta ferrite is located mainly at dendrite axes and has either a vermicular or lathy morphology. The proportion of the latter increases with the ratio Cr_{eq}/Ni_{eq}.

The results indicate that under conditions corresponding to a typical SMA welding only type *B* welds solidify in a manner in which the primary solidification of the delta ferrite is followed by a three-phase reaction between the liquid, delta ferrite and austenite. The austenite forms between ferrite dendrites peritectically or eutectically and grows into the melt and ferrite. This growth into the melt causes the segregation typical of austenitic solidification and may then enable the formation of interdendritic ferrite. The simultaneous or immediate growth of the austenite into the ferrite by an equiaxial or acicular mechanism results in a drastic decrease in the volume fraction of ferrite and in a partitioning between the austenite and residual ferrite. The compositional differences caused by solid-state transformation are greater than those generated by solidification, and their wave-length is much shorter.

Comparison of the results with those published in the literature shows that type *B* welds are resistant to hot cracking, but the risk of sigma embrittlement is obvious if the sum $Cr_{eq} + Ni_{eq}$ is too high.

ACKNOWLEDGMENTS

The authors thank Mr. S. Sivonen, Mr. L. Myllykoski, and the personnel of the Institute of Electron Optics, University of Oulu, for help in performing the experiments, especially the electron microprobe analysis.

REFERENCES

1. N. Suutala, T. Takalo, and T. Moisio: *Met. Trans. A*, 1979, vol. 10A, pp. 512-14.
2. T. Takalo, N. Suutala, and T. Moisio: *Met. Trans. A*, 1979, vol. 10A, pp. 1173-80.
3. N. Suutala, T. Takalo, and T. Moisio: *Met. Trans. A*, 1979, vol. 10A, pp. 1181-90.
4. A. L. Schaeffler: *Met. Progr.*, 1949, vol. 56, pp. 680 and 680B.
5. W. T. DeLong: *Weld. J.*, 1974, vol. 53, pp. 273s-86s.
6. F. C. Hull: *Weld. J.*, 1973, vol. 52, pp. 193s-203s.
7. E. Schürmann and J. Brauckmann: *Arch. Eisenhuettenwes.*, 1977, vol. 48, pp. 3-7.
8. J. Fridberg, L. E. Törndahl, and M. Hillert: *Jernkontorets Ann.*, 1969, vol. 153, pp. 265-76.
9. V. Siegel and M. Günzel: *Neue Huette*, part I, 1973, vol. 18, pp. 422-29; *Neue Huette*, part II, 1973, vol. 18, pp. 599-602.
10. A. E. Runov: *Weld. Prod.*, 1971, vol. 18, pp. 37-43.
11. H. Hoffmeister: *Schweissen Schneiden*, 1973, vol. 25, pp. 164-66.
12. H. Fredriksson: *Met. Trans.*, 1972, vol. 3, pp. 2989-97.
13. H. Fredriksson: *Solidification and Casting of Metals*, pp. 131-38, The Metals Society, London, 1979.
14. B. Leffler and S. Malm: Met. Technol., 1977, vol. 4, pp. 81-90.
15. H. Åström, B. Loberg, B. Bengston, and K. Easterling: *Met. Sci.*, 1979, vol. 10, pp. 225-34.
16. C. E. Lyman: *Weld. J.*, 1979, vol. 58, pp. 189s-94s.
17. A. Kyröläinen: *Svetsen*, 1978, vol. 37, pp. 119-24.
18. A. Kyröläinen: Private communication, University of Oulu, November 1979.
19. A. Bäumel: *Werkst. Korros.*, 1976, vol. 27, pp. 687-93.
20. F. C. Hull: *Weld. J.*, 1967, vol. 46, pp. 399s-409s.
21. V. Kujanpää, N. Suutala, T. Takalo, and T. Moisio: *Welding Res. Int.*, in press.
22. A. Bäumel: *Schweissen Schneiden*, 1967, vol. 19, pp. 264-69.
23. T. G. Gooch: *Weld. Inst. Res. Bull.*, 1974, vol. 15, pp. 183-88.
24. M. C. Bystram: *Br. Weld. J.*, 1956, vol. 3, pp. 41-46.